01 Aug 2023

Effect Of Shock Tunnel Geometry On Shockwave And Vortex Ring Formation, Propagation, And Head On Collision

Rachel L. Bauer

Emily M. Johnson

Alexander D. Douglas

Catherine E. Johnson
Missouri University of Science and Technology, johnsonce@mst.edu

Follow this and additional works at: https://scholarsmine.mst.edu/min_nuceng_facwork

Part of the Explosives Engineering Commons

Recommended Citation

Effect of shock tunnel geometry on shockwave and vortex ring formation, propagation, and head on collision ⊘

Special Collection: Shock Waves

Rachel L. Bauer ⬡ ; Emily M. Johnson ⬡ ; Alexander D. Douglas ⬡ ; Catherine E. Johnson ✉ ⬡

⬡ Check for updates

CrossMark

View Online

Export Citation

Articles You May Be Interested In

Treating heterotopic ossification with shockwaves.

J Acoust Soc Am (April 2009)

Shockwave-induced deformation of organic particles during laser shockwave cleaning

J. Appl. Phys. (August 2013)

Non-ideal explosive underwater explosion shockwave model

Physics of Fluids (August 2023)

Effect of shock tunnel geometry on shockwave and vortex ring formation, propagation, and head on collision

View Online   Export Citation   CrossMark

Rachel L. Bauer, (iD) Emily M. Johnson, (iD) Alexander D. Douglas, (iD) and Catherine E. Johnson[a] (iD)

AFFILIATIONS

Mining and Explosives Engineering Department, Missouri University of Science and Technology, Rolla, Missouri 65409, USA

Note: This paper is part of the special topic, Shock Waves.
[a]Author to whom correspondence should be addressed: catherine.johnson@mst.edu

ABSTRACT

Vortex ring research primarily focuses on the formation from circular openings. Consequently, the role of tunnel geometry is less understood, despite there being numerous research studies using noncircular shock tunnels. This experimental study investigated shockwaves and vortex rings from different geometry shock tunnels from formation at the tunnel opening to head on collision with another similarly formed vortex ring using schlieren imaging and statistical analysis. The velocity of the incident shockwave was found to be consistent across all four shock tunnel geometries, which include circle, hexagon, square, and triangle of the same cross-sectional area. The velocity was 1.2 ± 0.007 Mach and was independent of the tunnel geometry. However, the velocities of the resulting vortex rings differed between the shapes, with statistical analysis indicating significant differences between the triangle and hexagon vortex velocities compared to the circle. Vortex rings from the square and circle shock tunnels were found to have statistically similar velocities. All vortex rings slowed as they traveled due to corner inversion and air drag. All shock tunnels with corners produce a wobble in the vortex rings. Vortex rings interact with opposing incident shockwaves prior to colliding with each other. Vortex velocity before and after shock–vortex interaction was measured and evaluated, showing statistically similar results. Shock–vortex interaction slows the shockwave upon interaction, while the shock–shock interaction resulted in no change in shock velocity. Although the vortex rings travel at different velocities, all head-on vortex ring collisions produce a perpendicular shockwave that travels at 1.04 ± 0.005 Mach.

INTRODUCTION

Little, if any, previous research uses explosively driven shock tunnels to create and study vortex rings; however, research into blast induced traumatic brain injury, for example, has placed animals at the end of a shock tunnel in the vortex ring region.[1,2] Such explosively driven shock tunnels are often used to create shockwaves to replicate open field scenarios, but vortex rings are produced as a result of flow through the tunnel. These vortex rings are not produced in the open field. The impedance mismatch of the vortex ring to animals, or other external targets, can cause unwanted effects. Consequently, vortex ring formation from different tunnel geometries needs to be understood to mitigate possible negative effects in experimental designs.

Vortex rings are structures of rotating fluid, such as air or water, that rotate about a central axis. Formation of vortex rings can occur due to surface tension such as ripples across a pond,[3–6] buoyant plumes from volcanoes and smoke stacks,[4,5,7] and from flow separation.[4,5,8] This research specifically examines vortex rings that are formed from flow separation due to shear and boundary layers created in an explosively driven shock tunnel. Fluid is pushed through an opening resulting in the separation of the boundary layer at the edge of the opening.[4,8] Boundary layer separation causes the sheared layer to roll up into the vortex ring.[4,5] The ring will continue to travel in the original direction of impulse while rotating around a central core until impact with another vortex ring or solid surface. The Navier–Stokes equation has been used to computationally evaluate the travel and collision of circular vortex rings to determine how reconnected rings form.[9–12] Experimental circular vortex ring collisions have been studied using both air and water,[8,13–17] and this paper is a continuation of previous research conducted on circular vortex ring collisions in air, which have been shown to create shockwaves from vortex–vortex collision.[18] Other previous studies of vortex rings in air have shown the production of a wall shock due to vortex–wall collision.[16,19–24] Current research on shaped vortex rings focuses on rectangular rings such as those created at the exit of the engines of the F-22 Raptor fighter

jet.[25–27] Rectangular vortex rings have been found to dissipate quickly in air and deform into elliptical and circular shapes as they travel.[28–30] This paper will expand vortex ring research by including different geometry shock tunnels to evaluate the effect of geometry on vortex formation and travel.

The Reynolds number is a dimensionless value representing the ratio of inertial to viscous forces[31] and plays an important role in determining the outcome of vortex ring collisions.[20,27] Low Reynolds numbers result in the formation of new vortex rings, commonly referred to as reconnected rings.[32] The original rings collide, break apart, and then re-form to travel perpendicular to the original direction of motion.[32,33] High Reynolds numbers produce a turbulent cloud after collision as opposed to reconnected rings.[34,35] A high Reynolds number can also lead to faster dissipation of rings as more energy is required for the vortex rings to travel through turbulent flow from the high Reynolds number.[25,28,30]

Oblique shocks are an essential part of vortex ring formation and are the result of the pressure difference between the flow within the shock tunnel and the flow behind the vortex ring. The shock tunnel creates a high-pressure area that pushes the flow behind the vortex ring outwards, creating a low-pressure area.[36,37] The oblique shocks form in response to this pressure differential to equalize the pressure and prevent any further changes to the flow.[37] Once the oblique shock is formed, the flow upstream (the incident shock and vortex ring) can no longer be affected by the downstream flow.[13,38] These oblique shocks further confirm the area of low pressure behind the vortex rings and show that the vortex rings are no longer influenced by flow from the shock tunnel.

The effect of charge shape on blast waves has been studied and documented by various researchers,[39–42] but less research has been performed on the effect of tunnel shape on vortex rings. Charge shape alters the shape of the wave, specifically at the corners. In the far field, the shockwave becomes circular, and geometry of the charge is no longer significant.[40,41,43] Various geometry vortex rings transition to round cross sections at different rates depending on the geometry.[29,44] This research aims to study the shock–vortex and vortex–vortex interaction of different geometries prior to the vortices breaking down as well as the effect different geometries have on shockwave production.

This research examined the formation, travel, and interaction of shockwaves and vortex rings formed from four different geometrical tunnels using schlieren imaging and high-speed cameras. Circle, square, triangle, and hexagon shock tunnels, nonelectric lead line, and copper shock tunnel were used to create vortex rings. Statistical analysis and vortex velocity were used to determine which vortex rings were significantly different from the baseline circle geometry. Data from this work will determine the effect of tunnel geometry on vortex velocity, movement, and collision.

METHODOLOGY

Different geometry shock tunnels were used to study shock and vortex formation, travel, and their consequent impact with other shockwaves and vortex rings. The shockwaves were created using a 1.8 m length of nonelectric lead line with a velocity of detonation of approximately 2000 meters per second (m/s).[45] The nonelectric lead line was inserted approximately 0.71 meters (m) into a 1.27 cm diameter and 0.812 m-long copper pipe acting as a circular shock tunnel, shown in Fig. 1(b), to enable shockwave and vortex ring formation.
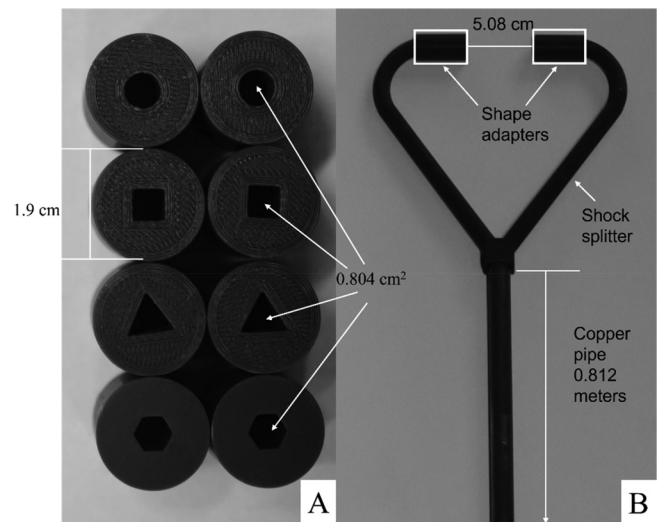

FIG. 1. (a) 3D printed shape adapters and (b) shape adapters connected to the 3D printed shock splitter and the copper pipe.

The pipe was connected to a 3D printed shock splitter used to split the shockwave and create the head-on collision. Circle, square, triangle, and hexagon shape adapters were used to create the shock tunnel exits that affect the boundary layer separation and vortex formation. The shock tunnel geometries were intentionally selected based on their distinct angles, acute, right, and obtuse. This deliberate choice allows for a comprehensive comparison with circular geometry. These shape adapter pieces in Fig. 1(a) keep the cross section of the opening area consistent at 0.804 cm^2 regardless of the shape selected.

A Phantom v2012 high-speed camera[46] with a frame rate of 100 000 frames per second (fps) and resolution of 384×384 captured images of the shock and vortex collisions using schlieren imaging. The experimental setup uses a two-mirror, Z-pattern schlieren setup with 135 mm diameter spherical mirrors. The mirrors have a focal length of 1 meter (m), and a point light source of 50 lumens is used in experimental testing. The test setup can be seen in Fig. 2. Figure 2(a) shows a top-down view of the test setup showing both spherical mirrors, the point light source, and test area. Figure 2(b) shows the test setup as viewed from spherical mirror 2, looking straight into the test area with a view of the point light source, shock splitter, and spherical mirror 1. Phantom Camera Control (PCC) software[47] was used to measure leading edge velocities of the shockwave and vortex rings.

Five tests of each geometry were performed using the same 3D printed apparatus and shape adapters. The resulting movement and collision of the shockwaves and vortex rings were observed and analyzed, specifically focusing on the geometry effects on shock and vortex ring formation, travel, and interactions.

RESULTS AND ANALYSIS

Shockwaves and vortex rings were produced using nonelectric lead line and copper shock tunnel. Schlieren imaging technology and a high-speed camera captured images of the formation, path of travel, and head-on collision of the vortex rings and resulting shockwave as shown successfully in previous studies.[18,44,48] Five repeats of each geometry (circle, hexagon, triangle, and square) were performed and
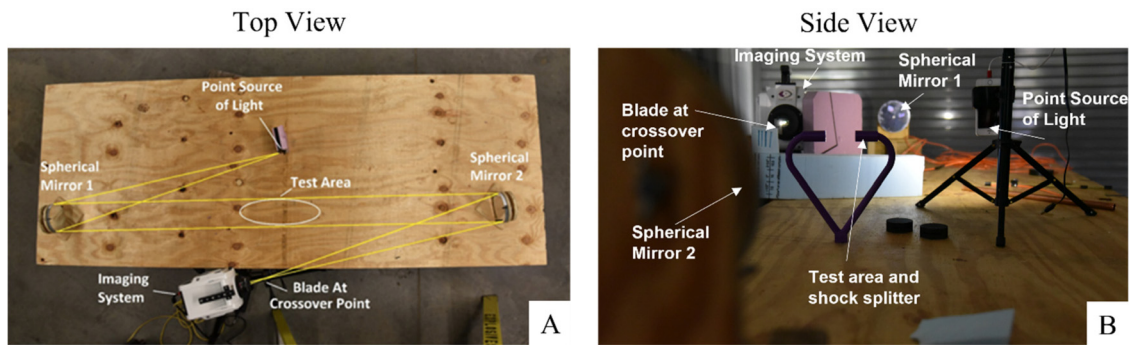
14 September 2023 13:48:13

FIG. 2. Schlieren test setup: (a) top view and (b) side view.

analyzed. Analysis includes each segment of the process from incident shockwave leaving the vortex tunnel, followed by the vortex ring, an oblique shock, and finally vortex collision.

Vortex ring characterization

To determine laminar or turbulent flow, the Reynolds number was calculated using Eq. (1), where U is the initial translation velocity of the vortex ring, D is the diameter of the vortex ring, and v is the kinematic viscosity of air calculated assuming ambient conditions of $22\,^\circ$C.[49] The diameter of the vortex ring and diameter of the shock tunnel can be considered the same immediately at the exit of the tube; thus, the shock tunnel diameter is used for the calculations,

$$Re = \frac{UD}{v}.$$ (1)

The diameter for the shock tunnel geometries was calculated using the incircle and circumcircle of each shape. The circumcircle passes through all vertices on the exterior of the shape, the incircle is the largest circle that can be inscribed in the shape, and an example for the square is shown in Fig. 3. The Reynolds number was then calculated using incircle and circumcircle values. All Reynolds number values indicated turbulent flow as the values were all greater than 2000 as seen in Table I.
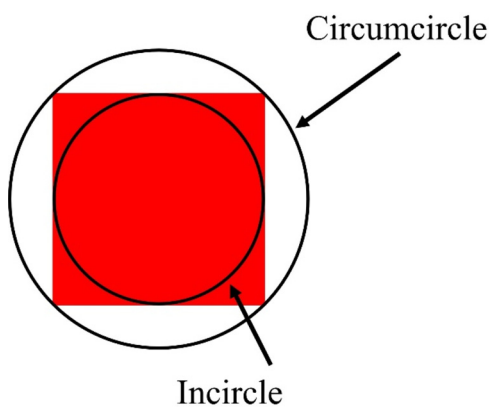

FIG. 3. Incircle and circumcircle of a square used to calculate Reynolds number.

TABLE I. Reynolds number of each geometry.

Geometry	Incircle Re	Circumcircle Re
Square	8.4×10^4	1.2×10^5
Hexagon	1.03×10^5	1.66×10^5
Triangle	3.3×10^4	2.1×10^5
Circle	9.3×10^4	9.3×10^4

Based on the Reynolds number, all shock tunnels produce turbulent flow, which can result in shockwaves and vortex rings of increased velocity when compared to laminar flow. The mixing of air in turbulent flow results in strong incident shockwaves for each geometry shock tunnel. The high-speed imagery shows that all four geometries produce an incident shockwave, followed by the vortex rings and then an oblique shock.

The exit of vortex rings from the shape adapters in all four geometries results in the formation of oblique shocks, which can be characterized by their Mach numbers and calculated using Eq. (2). The incident shockwave is the first to leave the shape adapter, followed by the vortex ring and then the oblique shock,

$$M_\infty = \frac{1}{\sin \propto}.$$ (2)

M_∞ is the Mach of the oblique shock, while $\sin \propto$ is the angle the shock makes as it exits the tunnel, seen in Fig. 4. This shock forms by reflection off the walls of the 3D printed shaped adapters. A similar phenomenon is seen in converging–diverging nozzles of rocket
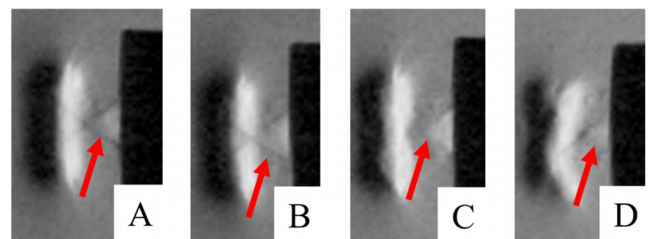

FIG. 4. Oblique shocks of each geometry at 60 μs: (a) circle, (b) hexagon, (c) square, and (d) triangle.

engines.[50–52] The circle has the highest Mach number for the oblique shock (1.83) because it has no corners that affect the flow. All shock tunnels with corners produce vortex rings that wobble and create turbulent flow, creating lower Mach numbers. The undisturbed flow from the circular shock tunnel allows for stronger oblique shocks with higher Mach numbers. Flow disturbance in the hexagon, square, and triangle shock tunnels is evident in the wobble of the vortex rings showing the ring movement due to tunnel geometry. The hexagon shock tunnel has the next highest Mach number at 1.74. This shock tunnel has obtuse angles that make the tunnel similar to the circle, thus similar Mach numbers. Right angles in the geometry of the square decrease the Mach number of the oblique shock to 1.70, while the acute angles of the triangle result in a Mach number of 1.59. The triangle has the largest perimeter of all the geometries, thus a slower moving oblique shock.

Slower oblique shocks in geometries of a larger perimeter highlight the interplay between geometry, flow regime, and the resulting behavior of shockwaves and vortex rings. The turbulent flow indicated by the Reynolds numbers contributes to the generation of stronger shockwaves and vortex rings. On the other hand, the presence of corners and the resulting flow disturbances affect the dynamics of the vortex rings, leading to variations in the Mach numbers of the oblique shocks.

The correlation between the Mach number and Reynolds number demonstrates that different geometries influence both the flow regime (turbulent or laminar) and the compressibility effects (high or low Mach number) within the shock tunnels. These factors collectively impact the behavior and characteristics of the generated shockwaves and vortex rings.

Vortex ring propagation

All rings except the one produced from the circular shock tunnel wobble or invert as they travel toward each other as seen in Fig. 5. The geometries with the most pronounced wobble are those with corners of 90° or less, the square and triangle. The vortex ring from the circular shock tunnel is the only one without a wobble as there are no corners and the geometry is uniform. The vortex from the hexagon shock tunnel has obtuse corners and wobbles slightly, but not as much as the other geometries. All the wobbles of the vortex rings can be seen in Fig. 5 taken at 40 microseconds (μs), 60, and 80 μs for each geometry. The wobble of the vortex rings creates air drag, causing the rings to slow as they travel. Vortex rings from the square, triangle, and hexagon shape adapters all travel slower than those from the circle prior to collision due to this wobble and air drag.

The corner inversion phenomenon of the square and triangle vortex rings is visually depicted in Fig. 6. It is essential to clarify that the setup for these images differs from the experimental setup and was exclusively designed to enhance visual understanding while conducting the analysis of the experimental tests. These additional images were created to provide a clearer visualization of the corner inversion effect without directly influencing the actual experimental measurements. To facilitate this visual analysis, an additional square shock tunnel with a cross-sectional area of 3.6 cm^2 and a triangle shock tunnel with a cross-sectional area of 3.2 cm^2 were 3D printed.

Square shaped vortex rings have been shown to not hold their shape well, as the vortex inversion causes the corners to flatten and create a shape known as a squircle.[53] The squircle is a cross between a square and circle[54] with rounded edges rather than corners like a square.

In Figs. 6(a)–6(c), the propagation of the vortex ring from the square shock tunnel is observed as it undergoes a transition, eventually transforming into a squircle. During this transformation, the cross-sectional area of the vortex ring increases, leading to a decrease in its velocity. Similarly, in Figs. 6(e) and 6(f), the vortex ring from the triangle shock tunnel is shown going through the corner inversion process. Initially resembling a triangle with the apex pointing downward, the vortex ring gradually transitions to a configuration with the apex pointing upward. The images in Fig. 6 complement the experimental
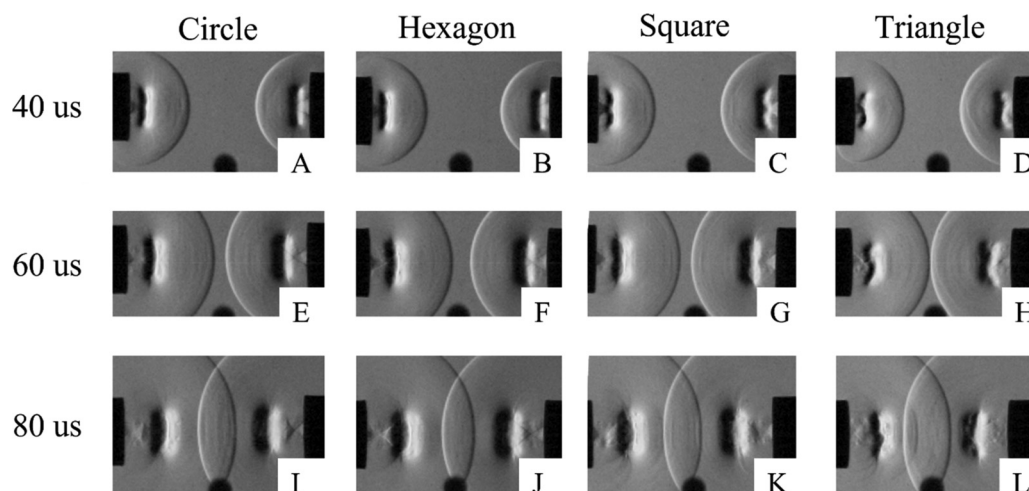
FIG. 5. The wobble of each vortex ring at 40, 60, and 80 μs. (a) The circle vortex rings at 40 μs, (b) hexagon vortex rings at 40 μs, (c) square vortex rings at 40 μs, (d) triangle vortex rings at 40 μs, (e) circle vortex rings at 60 μs, (f) hexagon vortex rings at 60 μs, g square vortex rings at 60 μs, (h) triangle vortex rings at 60 μs, (i) circle vortex rings at 80 μs, (j) hexagon vortex rings at 80 μs, (k) square vortex rings at 80 μs, and (l) triangle vortex rings at 80 μs.
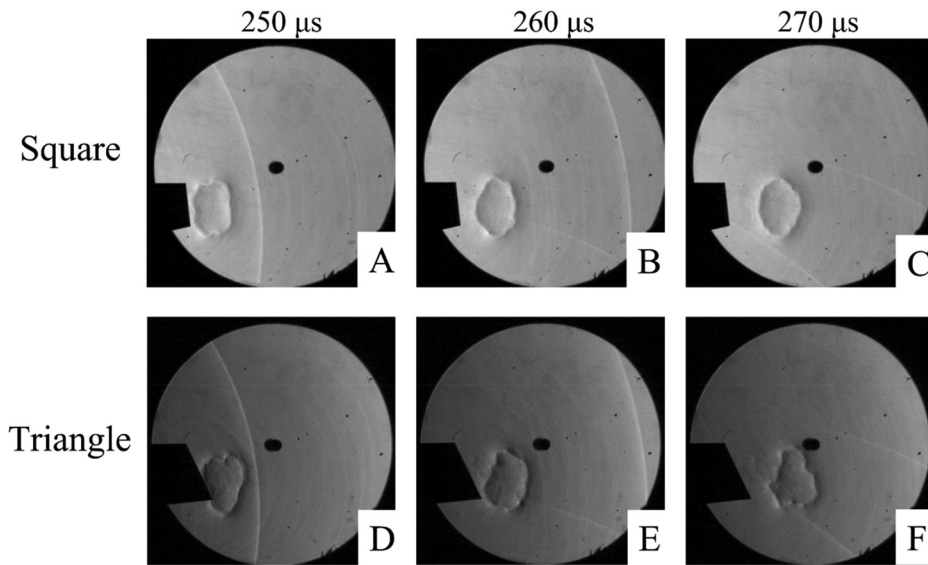
FIG. 6. Vortex rings from the square and triangle shock tunnels traveling and going through corner inversion. (a) The vortex ring at 250 μs in a square shape, (b) the vortex ring at 260 μs inverting to the squircle, (c) the vortex at 270 μs with rounded corners, (d) triangle vortex ring leaving the shock tunnel, (e) triangle vortex ring in the middle of corner inversion, and (f) triangle vortex ring after going through corner inversion.

data and contribute to a comprehensive understanding of the wobbling phenomenon exhibited by vortex rings in square and triangle geometries.

Vortex rings generated from geometries with corners exhibit a distinct phenomenon known as "corner inversion," which leads to the observed wobbling as the vortex rings travel. In Fig. 7, each vortex ring used in this study is shown alongside the corresponding corner inversion, created in Fusion 360, which plays a crucial role in inducing the wobble.

In circular geometries [Fig. 7(a)], the flow velocities around the entire vortex ring are relatively constant. As a result, there is no corner inversion, and the vortex ring maintains a stable and uniform trajectory during its travel.

In geometries with corners [Figs. 7(b)–7(d)], the fluid inside the vortex ring flows faster in the regions around the corners compared to the rest of the ring. This non-uniform flow creates areas of the ring that propagate faster than the surrounding sections. As the vortex ring advances, the faster-moving regions propagate faster than the slower-moving portions, leading to corner inversion. The corner inversion causes the vortex ring to exhibit a wobbling motion as it moves through the medium.

This wobbling phenomenon is a result of the fluid dynamics induced by the corners in the geometries. The presence of corners can cause flow separation and pressure gradients, resulting in a non-uniform distribution of velocities along the vortex ring's circumference
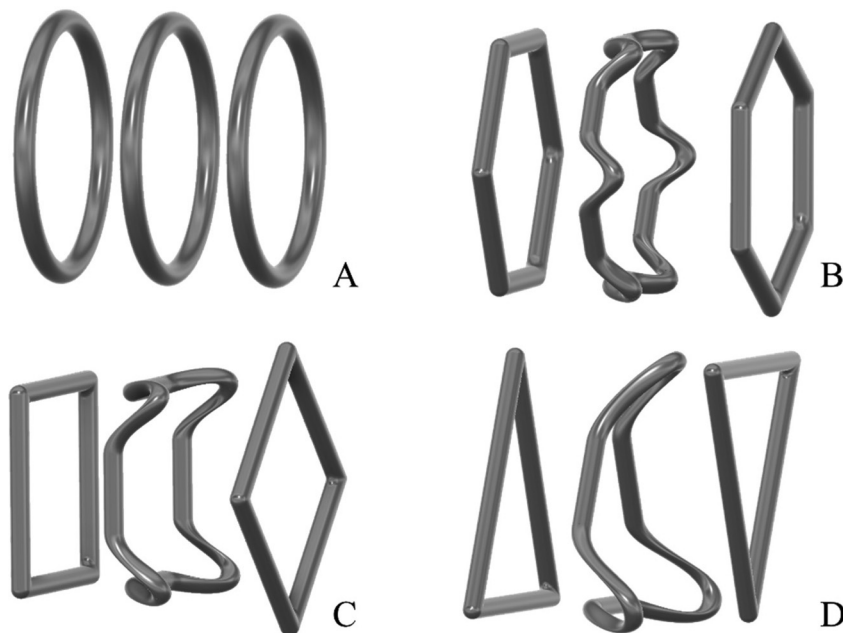

FIG. 7. Corner inversion of each vortex ring: (a) circle, (b) hexagon, (c) square, and (d) triangle.

where fluid flows faster at the corners. Consequently, the vortex ring experiences imbalanced forces, leading to corner inversion and subsequent wobbling. The presence of corners in non-circular vortex rings can cause non-uniform velocities throughout the circumference of the ring. This can lead to wobbling and deformation of the ring over time as shown in previous literature.[28,55,56] The sharp corners of rectangular or square vortex rings can attain higher corner velocities than circular vortex rings, which can lead to corner-induced deformations and wobbling.[30,57–59] Previous research has shown the existence of a wobble or corner inversion in non-circular vortex rings.[25,26,44,60,61] Square and rectangular rings have been shown to transform into a circle,[28–30] similar to the squircle found in this research. This research shows a comparative analysis between shock tunnels of different geometries not seen in previous literature and includes vortex formation from obtuse angled geometries.

Area was kept constant for all geometries, meaning that perimeter can be used as a variable. As the perimeter increases, the geometries become less related to the circle. Of the various geometries, the triangle has the largest perimeter of 4.09 cm and is the least like the circle, which has the lowest perimeter of 3.18 cm. The square has a larger perimeter (3.59 cm) than the circle and the hexagon, but statistical analysis showed the vortex rings from the square shock tunnel were not significantly different than those from the circle. While the hexagon is most like the circle in terms of perimeter (3.34 cm), the vortex rings from the hexagon shock tunnel show a significant difference from the circle. The large perimeter of the triangle causes the vortex rings to slow and become significantly different from the circle. Vortex rings from the hexagon shock tunnel also have a larger perimeter and slow as they travel. The perimeter of the square is larger than the circle, but the transition of the square to the squircle decreases these effects resulting in vortex rings that are not significantly different than those from the circle shock tunnel.

Figure 8 presents a comprehensive comparison, using box and whisker plots, of measured velocities for the shockwaves and vortex rings from different geometry shock tunnels. To facilitate easy comparison, the y-axis displays the average velocity for the circle for each metric displayed as well as a solid line for a Mach of 1 to clearly show super and subsonic velocities. The figure clearly demonstrates that the shock velocities of all geometries are similar, validating the earlier

statement that shock velocity is independent of tunnel geometry. In contrast, the vortex velocities exhibit significant differences among the geometries, as supported by both the statistical analysis and the visual representation provided in Fig. 8. The figure visually conveys that the vortex velocities not only differ from the circular shock tunnel but also display greater variability and uncertainty. This is indicated by the larger boxes and whiskers associated with the vortex velocities, signifying the spread of data points around the mean velocity values for each geometry. The significance of these findings regarding vortex velocities and their dependency on tunnel geometry will be discussed in subsequent paragraphs.

The incident shockwaves travel at an average velocity of 1.2 ± 0.007 Mach upon leaving the shape adapters, showing consistency in the experimental setup and shockwaves that are independent of tunnel geometry. Figure 9 shows the incident shock velocities from the left and right shape adapters for the five repeated tests. The similarity between the velocities of all incident shockwaves is shown as well as the minimal deviation indicating consistency in the measurements.

The vortex rings leave the shape adapters an average of $27 \pm 2\mu s$ after the incident shockwaves. The velocity of the vortex rings was measured as the rings left the shape adapters and then again prior to impact.

Vortex velocity was broken down into two separate stages, the vortex leaving the shape adapter and immediately prior to collision. Velocities were calculated for the left and right vortex rings immediately after leaving the shape adapters, but before impacting the opposing shockwave. Velocities were then calculated for the vortex rings after passing through the opposing shockwave but prior to head-on collision with the opposite vortex ring. The same number of frames was used for both calculations. An analysis of variance (ANOVA) was performed on the data first, and a p-value of less than 0.05 was used to indicate statistical significance. If the ANOVA indicated a statistical significance, an independent samples t-test with a threshold of $p < 0.05$ was used to determine if there was a statistically significant difference between the specific shock tunnel geometries. In both cases, the analysis of variance showed that a significant difference was present between the geometries.

The circle was used as the baseline geometry; an analysis of variance (ANOVA) and t-tests were run to compare vortex velocity of
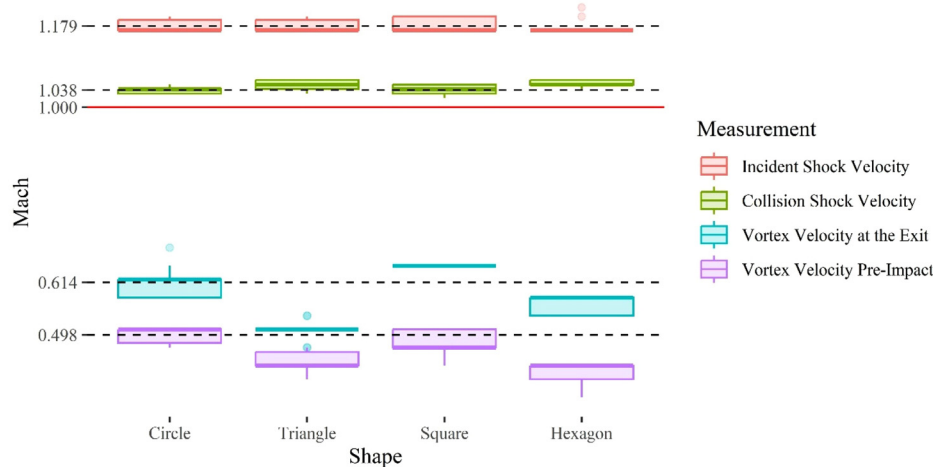

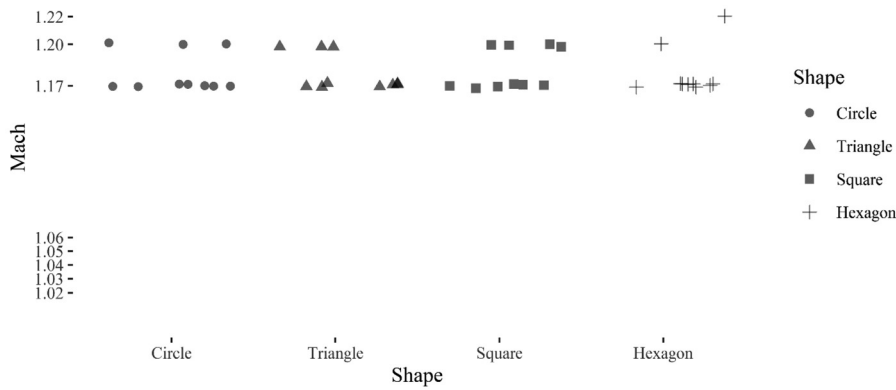FIG. 8. Velocity measurements of the shockwaves and vortex rings.

FIG. 9. Incident shock velocities from the shape adapters.

different geometries to the circle. The two-tailed t-test p-value was used to account for the total range of statistical differences. Both the left and right vortex rings showed the same results, the triangle and hexagon were significantly different from the circle, but the square was not. These results were consistent for both the vortex velocities leaving the shape adapters and the velocities immediately before head-on collision. After the shock–vortex interaction, the vortex rings decrease in velocity, but triangle and hexagon shape adapters are still significantly different than the circle. Velocities of the vortex rings after leaving the shape adapter can be seen in Fig. 10, while velocities of the vortex rings prior to head-on collision can be seen in Fig. 11. Vortex rings generated from explosively driven shock tunnels exhibit structural integrity and remain cohesive even in the presence of strong fluid flows, such as the opposing shockwaves, without undergoing significant deformation or disintegration, allowing for velocity measurements before and after shock–vortex interaction.

To assess the statistical significance of these observations, a 95% confidence interval was used in conjunction with t-tests. As the square, triangle, and hexagon vortex rings traveled, their confidence intervals increased, indicating an elevation in uncertainty and variability. This increase in variability was attributed to the shock–vortex interaction and the wobbling motion of the vortex rings.

The interaction between the shockwaves and vortex rings led to the introduction of turbulence, resulting in slower velocities and reduced stability of the vortex rings. The circular vortex rings, on the other hand, did not exhibit an increase in confidence intervals since

they did not experience the same wobbling motion caused by corners in the geometry. However, they still showed a decrease in velocity due to the shock–vortex interaction.

Vortex–vortex collision

As the vortex rings are traveling toward each other, they begin to trap air between them. Air is continuously pushed into the space between the rings due to the vortex ring rotation. The increase in pressure of the trapped air causes a pressure gradient as the air between the rings has a much higher pressure than the surrounding air. Once the rings collide and break, the high-pressure air is released and creates a shockwave. This pressure gradient was verified through experimental studies and simulations by these authors previously,[18] and the mechanism of formation for the shockwave remains the same for different geometry shock tunnels. Figure 12 shows the expanding shockwave as a result of the vortex ring collisions.

As the incident shockwaves travel, the region behind the wave has a lower density. The vortex rings travel in this area of low density up until the head-on collision. Low density air facilitates the formation of the shockwave as the two vortex rings collide. The low-density air allows for the fast propagation of the shockwave once the vortex rings collide, allowing the wave to travel faster and more efficiently than that in higher density air. As the subsonic rings collide, they produce a shockwave that travels through the low-density region produced by the incident shockwaves.
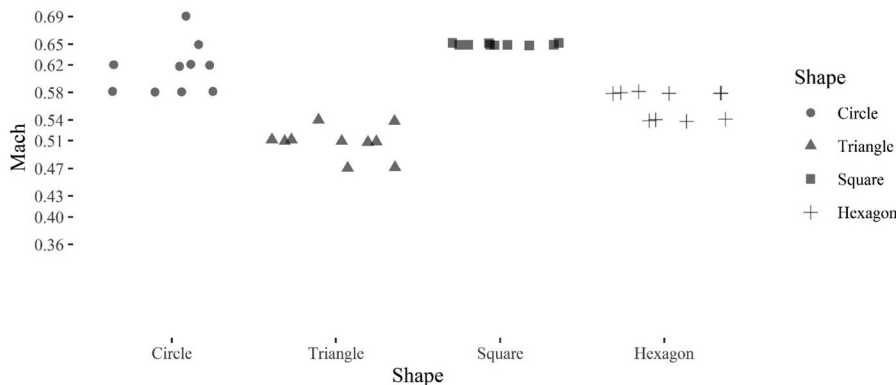

FIG. 10. Vortex velocity leaving the shape adapters.
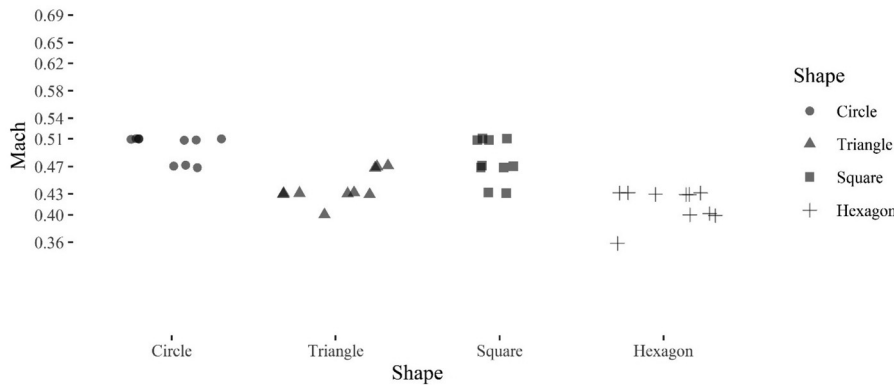
14 September 2023 13:48:13

FIG. 11. Vortex velocity prior to impact.

Vortex rings have much more variability and randomness as they travel when compared to the incident shockwave and shockwave from vortex collision. All the incident shockwaves were formed from a consistent method, the non-electric lead line. The shockwave produced from vortex ring collision was formed due to the release of high-pressure air and breaking of vortex rings. The rings travel and wobble differently in each test so the collisions are never the same. In each experimental trial, vortex collision results in the formation of a region of high-pressure air and release of a shockwave. Shockwave velocity after collision shows no statistical difference between geometries tested. A comparison of the incident shock velocities and collision shock velocities can be seen in Fig. 13.

When comparing the average vortex collision shock velocities, there is no statistically significant difference observed among the geometries tested. The circle, square, triangle, and hexagon tunnels all exhibit similar velocities for the shockwaves generated after the vortex rings collide. Similarly, when examining the average incident shock velocities, there is no substantial variation among the geometries tested. The incident shockwaves are formed from non-electric lead line, which consistently produces incident shockwaves with comparable velocities across the different geometry tunnels.

These results indicate that, despite the variations in vortex ring travel and wobbling patterns observed in each test, the collisions consistently result in the formation of a high-pressure air region and subsequent formation of a shockwave. The similarities in both incident and collision shock velocities across the different geometries suggest that the velocity of the resulting shockwaves is independent of shape of the shock tunnel.

This study demonstrates that vortex ring travel exhibits more variability and randomness compared to the incident shockwave. The head-on collision of vortex rings consistently leads to the formation of high-pressure air regions and the release of shockwaves, with similar velocities observed across the circle, square, triangle, and hexagon geometries. These findings highlight the robustness of the vortex collision phenomenon and suggest that other factors, such as angles or perimeter of the shapes, should be explored to identify potential correlations with vortex wobble or velocity characteristics.

CONCLUSION

This paper analyzed the formation, propagation, and head on collision of shockwaves and vortex rings produced by different geometry shock tunnels through schlieren imaging and statistical analysis. Previous research has shown that vortex ring collisions produce a shockwave, but vortices produced by different geometry shock tunnels have not been studied. Explosively driven shock tunnels created incident shockwaves of consistent velocity with resulting vortex rings. The vortex rings of different geometries traveled at different velocities and were analyzed for statistical differences. The triangle and hexagon vortex ring velocities were found to be significantly different than the circle vortex rings. The vortex rings from square, triangle, and hexagon geometry shock tunnels travel slower than the circle, but still create a shockwave upon collision with no statistical difference in shock velocity.

Vortex rings with either acute, right, or obtuse corners will invert and appear to wobble in schlieren images. Geometries with smaller angled corners, such as triangles and squares, will have a more pronounced wobble than a hexagon with obtuse angles. The wobble of the vortex rings is due to corner inversion of the rings, which results in increased air drag. Air drag on the vortex rings results in decreased velocity.
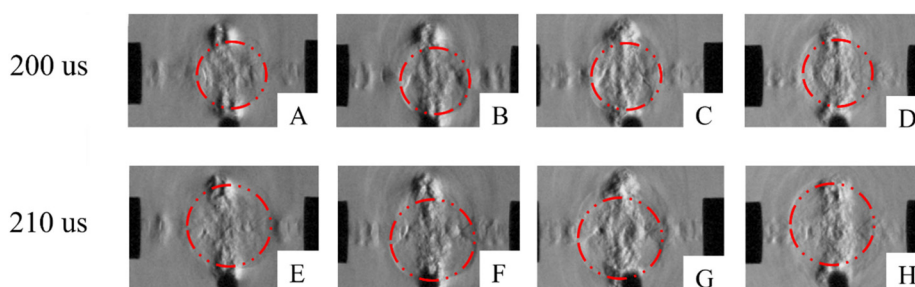

FIG. 12. (a) The circle vortex ring collision at 200 μs, (b) hexagon vortex ring collision at 200 μs, (c) square vortex ring collision at 200 μs, (d) triangle vortex ring collision at 200 μs, (e) circle vortex ring expanding shockwave at 210 μs, (f) hexagon vortex ring expanding shockwave at 210 μs, (g) square vortex ring expanding shockwave at 210 μs, and (h) triangle vortex ring expanding shockwave at 210 μs.
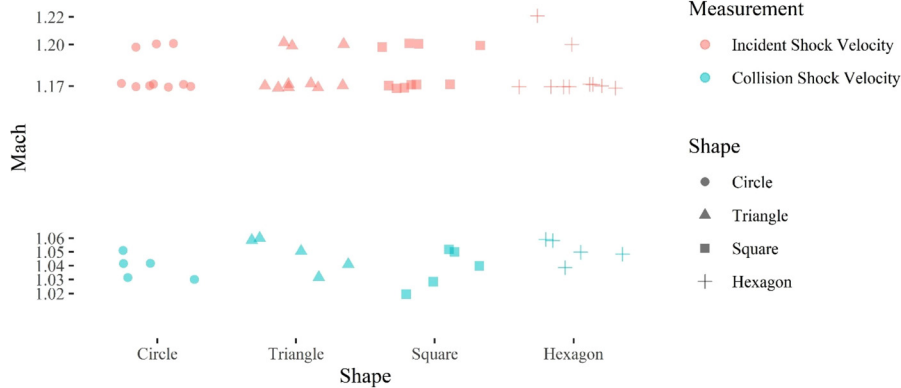
FIG. 13. Incident and collision shock velocities.

As the vortex rings approach a head-on collision, high-pressure air becomes trapped between the rings. The collision results in a release of air moving to equilibrium causing a shockwave. Vortex rings with significantly different velocities and wobbliness all produced statistically similar perpendicular shockwaves after head on collisions.

These results show statistical differences in vortex formation and interaction when area is held constant but with different geometries. Future work will investigate the effect of constant perimeter on the formation of shockwaves and associated vortex rings when formed from explosively driven shock tunnels in addition to the pressure produced by vortex ring collision with a wall. Additional research could also examine how factors, such as temperature and shock tunnel material, will impact the dynamics of vortex ring collisions.

ACKNOWLEDGMENTS

AUTHOR DECLARATIONS
Conflict of Interest

The authors have no conflicts to disclose.

Author Contributions

Rachel Bauer: Conceptualization (equal); Data curation (lead); Formal analysis (lead); Methodology (equal); Validation (equal); Visualization (lead); Writing – original draft (lead); Writing – review & editing (equal). **Emily Johnson:** Methodology (equal); Validation (equal); Writing – review & editing (equal). **Alexander D. Douglas:** Formal analysis (equal); Methodology (supporting); Validation (equal); Writing – review & editing (equal). **Catherine E. Johnson:** Conceptualization (equal); Methodology (equal); Project administration (lead); Resources (lead); Supervision (lead); Validation (equal); Writing – review & editing (equal).

DATA AVAILABILITY

The data that support the findings of this study are available within the article.

REFERENCES

[1]D. V. Reneer, R. D. Hisel, J. M. Hoffman, R. J. Kryscio, B. T. Lusk, and J. W. Geddes, "A multi-mode shock tube for investigation of blast-induced traumatic brain injury," J. Neurotrauma **28**(1), 95–104 (2011).

[2]B. Rutter *et al.*, "Shock wave physics as related to primary non-impact blast-induced traumatic brain injury," Mil. Med. **186**(Suppl 1), 601–609 (2021).

[3]J. S. Lee, S. J. Park, J. H. Lee, B. M. Weon, K. Fezzaa, and J. H. Je, "Origin and dynamics of vortex rings in drop splashing," Nat. Commun. **6**, 8187 (2015).

[4]P. S. Krueger, A. A. Moslemi, J. T. Nichols, I. K. Bartol, and W. J. Stewart, "Vortex rings in bio-inspired and biological jet propulsion" Adv. Sci. Technol. **58**, 237–246 (2008).

[5]A. Glezer, "The formation of vortex rings," Phys. Fluids **31**(12), 3532 (1988).

[6]K. Shariff and A. Leonard, "Vortex rings," Annu. Rev. Fluid Mech. **24**(1), 235–279 (1992).

[7]L. Gao and S. C. M. Yu, "Vortex ring formation in starting forced plumes with negative and positive buoyancy," Phys. Fluids **28**(11), 113601 (2016).

[8]M. Gharib, E. Rambod, and K. Shariff, "A universal time scale for vortex ring formation," J. Fluid Mech. **360**, 121–140 (1998).

[9]H. Feng, "On three-dimensional Navier-Stokes equations with axi-symmetric vortex rings as initial vorticity," Ph.D. dissertation, University of Minnesota Twin Cities, 2013.

[10]S. Stanaway, K. Shariff, and F. Hussain, "Head-on collision of viscous vortex rings," in Center for Turbulence Research Proceedings of the Summer Program, 1988; available at https://ui.adsabs.harvard.edu/abs/1988stun.proc.. 287S/abstract.

[11]K. Ishii, K. Kuwahara, and C. H. Liu, "Navier—Stokes calculations for vortex rings in an unbounded domain," Comput. Fluids **22**(4), 589–605 (1993).

[12]H. Tryggeson, "Analytical vortex solutions to the Navier–Stokes equation," Doctoral thesis (Växjö University Press, Växjö, 2007).

[13]J. P. Baird, "Supersonic vortex rings," Proc. R. Soc. A **409**(1836), 59–65 (1987).

[14]T. T. Lim and T. B. Nickels, "Instability and reconnection in the head-on collision of two vortex rings," Nature **357**(6375), 225 (1992).

[15]A. Mishra, A. Pumir, and R. Ostilla-Mónico, "Instability and disintegration of vortex rings during head-on collisions and wall interactions," arXiv:2107.12324 (2021).

[16]T. H. New, S. Shi, and B. Zang, "Some observations on vortex-ring collisions upon inclined surfaces," Exp. Fluids **57**(6), 109 (2016).

[17]N. K. Jha and R. N. Govardhan, "Interaction of a vortex ring with a single bubble: Bubble and vorticity dynamics," J. Fluid Mech. **773**, 460–497 (2015).

[18]R. L. Bauer *et al.*, "Shock wave formation from head-on collision of two subsonic vortex rings," Sci. Rep. **12**, 7492 (2022).

[19]S. Poudel, L. Chandrala, D. Das, and A. De, "Characteristics of shock tube generated compressible vortex rings at very high shock Mach numbers," Phys. Fluids **33**(9), 096105 (2021).

[20]Z.-Y. Li, Y. Xu, L.-H. Feng, and J.-J. Wang, "Synthetic jet vortex rings imping-ing onto a porous wall: Reynolds number effect," Int. J. Heat Mass Transfer **137**, 951–967 (2019).

[21]R. Mariani, K. Kontis, and N. Gongora-Orozco, "Head on collisions of com-pressible vortex rings on a smooth solid surface: Effects of surface distance var-iation," Shock Waves **23**(4), 381–398 (2013).

[22]T. H. New and B. Zang, "Head-on collisions of vortex rings upon round cylin-ders," J. Fluid Mech. **833**, 648–676 (2017).

[23]T. H. New, J. Long, B. Zang, and S. Shi, "Collision of vortex rings upon V-walls," J. Fluid Mech. **899**, A2 (2020).

[24]T. Minota, "The flow-field around a small square plate interacting with the vor-tex flow released from a shock tube," in *Shock Waves*, edited by Z. Jiang (Springer, Berlin, Heidelberg, 2005), pp. 677–682.

[25]J. J. Ai, S. C. M. Yu, A. W.-K. Law, and L. P. Chua, "Vortex dynamics in start-ing square water jets," Phys. Fluids **17**(1), 014106 (2005).

[26]A. Ghasemi, V. Roussinova, R. M. Barron, and R. Balachandar, "Large eddy simulation of the near-field vortex dynamics in starting square jet transitioning into steady state," Phys. Fluids **28**(8), 085104 (2016).

[27]M. Xu, A. Pollard, J. Mi, F. Secretain, and H. Sadeghi, "Effects of Reynolds number on some properties of a turbulent jet from a long square pipe," Phys. Fluids **25**(3), 035102 (2013).

[28]A. Ghasemi, B. A. Tuna, and X. Li, "Curvature-induced deformations of the vortex rings generated at the exit of a rectangular duct," J. Fluid Mech. **864**, 141–180 (2019).

[29]A. Bejan, S. Ziaei, and S. Lorente, "Evolution: Why all plumes and jets evolve to round cross sections," Sci. Rep. **4**(1), 4730 (2015).

[30]A. Ghasemi, B. A. Tuna, and X. Li, "Viscous diffusion effects on the self-induced distortions of rectangular vortex rings," Phys. Fluids **30**(12), 124101 (2018).

[31]See https://www.grc.nasa.gov/www/BGH/reynolds.html for "Reynolds Number" (accessed November 29, 2021).

[32]M. Cheng, J. Lou, and T. T. Lim, "Collision and reconnection of viscous elliptic vortex rings," Phys. Fluids **31**(6), 067107 (2019).

[33]P. Chatelain, D. Kivotides, and A. Leonard, "Reconnection of colliding vortex rings," Phys. Rev. Lett. **90**(5), 054501 (2003).

[34]D. Barkley, "Theoretical perspective on the route to turbulence in a pipe," J. Fluid Mech. **803**, P1 (2016).

[35]B. Rehm, D. Consultant, A. Haghshenas, A. S. Paknejad, and J. Schubert, "Chapter two—Situational problems in MPD," in *Managed Pressure Drilling*, edited by B. Rehm, J. Schubert, A. Haghshenas, A. S. Paknejad, and J. Hughes (Gulf Publishing Company, 2008), pp. 39–80.

[36]See https://www.grc.nasa.gov/www/k-12/airplane/oblique.html for "Oblique Shock Waves" (accessed January 20, 2023).

[37]S. Kitajima, J. Iwamoto, and E. Tamura, "A study on the behavior of shock wave and vortex ring discharged from a pipe," in FLUCOME 2009, 10th International Conference on Fluid Control, Measurements, and Visualization, Moscow, Russia, 17–21 August 2009.

[38]R. Mariani, *Compressible Vortex Rings and Their Interaction with Stationary Surfaces* (University of Manchester, 2012).

[39]K. R. Williams, "Investigating the focusing effect of charge geometry with com-puter simulations, witness plates, and high-speed videography," Ph.D. thesis (Missouri University of Science and Technology, Missouri, 2021).

[40]Y. Shi, N. Wang, J. Cui, C. Li, and X. Zhang, "Experimental and numerical investigation of charge shape effect on blast load induced by near-field explosions," Process Saf. Environ. Prot. **165**, 266–277 (2022).

[41]K. Williams and C. E. Johnson, "Investigating anisotropic blast wave parame-ters near the explosive-air boundary using computer simulation and experi-mental techniques with varying charge geometry," J. Appl. Phys. **130**(20), 205902 (2021).

[42]K. Williams and C. E. Johnson, "Evaluating blast wave overpressure from non-spherical charges using time of arrival from high-speed video," Propellants, Explos., Pyrotech. **8**(7), e202200346 (2023).

[43]W. Xiao, M. Andrae, and N. Gebbeken, "Effect of charge shape and initiation configuration of explosive cylinders detonating in free air on blast-resistant design," J. Struct. Eng. **146**(8), 04020146 (2020).

[44]M. Kainuma, M. Havermann, M. Sun, and K. Takayama, "Effects of the shock tube open-end shape on vortex loops released from it," in *Shock Waves*, edited by Z. Jiang (Springer, Berlin, Heidelberg, 2005), pp. 505–510.

[45]Dyno Nobel, see https://www.dynonobel.com/~/media/Files/Dyno/ResourceHub/Technical%20Information/North%20America/Initiation%20Systems/NONEL/Lead%20Line.pdf for "Nonel Lead Line" (accessed December 02, 2021).

[46]See https://www.phantomhighspeed.com/products/cameras/ultrahighspeed/%20v2012 for "Phantom v2012" (accessed September 4, 2022).

[47]See https://www.phantomhighspeed.com/resourcesandsupport/phantomresources/pccsoftware for "PCC Software" (accessed April 13, 2022).

[48]T. Mizukaki, "Visualization of compressible vortex rings using the background-oriented schlieren method," Shock Waves **20**(6), 531–537 (2010).

[49]See https://www.engineeringtoolbox.com/air-absolute-kinematic-viscosity-d_601.html for "Air—Dynamic and Kinematic Viscosity" (accessed November 29, 2021).

[50]L. Hirschberg, S. J. Hulshoff, J. Collinet, C. Schram, and T. Schuller, "Vortex nozzle interaction in solid rocket motors: A scaling law for upstream acoustic response," J. Acoust. Soc. Am. **144**(1), EL46–EL51 (2018).

[51]L. Qin, Y. Xiang, S. Qin, and H. Liu, "On the structures of compressible vortex rings generated by the compressible starting jet from converging and diverging nozzles," Aerosp. Sci. Technol. **106**, 106188 (2020).

[52]J. Zhu and S. Elbel, "CFD simulation of vortex flashing flows in convergent-divergent nozzles," 2018.

[53]F. F. Grinstein, "Vortex dynamics and entrainment in rectangular free jets," J. Fluid Mech. **437**, 69–101 (2001).

[54]J. C. Stapel and W. P. Medendorp, "Panoramic uncertainty in vertical perception," Front. Integr. Neurosci. (published online 2021).

[55]L. Vega, "The dynamics of vortex filaments with corners," Commun. Pure Appl. Anal. **14**(4), 1581–1601 (2015).

[56]"Vortex Rings from notched nozzles." arXiv:1708.05639 (2015).

[57]L. Wang, L.-H. Feng, J.-J. Wang, and T. Li, "Evolution of low-aspect-ratio rect-angular synthetic jets in a quiescent environment," Exp. Fluids **59**(6), 91 (2018).

[58]R. Belanger, D. W. Zingg, and P. Lavoie, "Vortex structure of a synthetic jet issuing into a turbulent boundary layer from a finite-span rectangular orifice," AIAA Paper No. AIAA 2020-1815, 2020.

[59]Y. Xiang, L. Qin, S. Qin, and H. Liu, "Circulation production model and uni-fied formation number of compressible vortex rings generated by a shock tube," Phys. Fluids **35**(3), 036121 (2023).

[60]J. C. Straccia and J. A. N. Farnsworth, "Axis switching in low to moderate aspect ratio rectangular orifice synthetic jets," Phys. Rev. Fluids **6**(5), 054702 (2021).

[61]R. S. Miller, C. K. Madnia, and P. Givi, "Numerical simulation of non-circular jets," Comput. Fluids **24**(1), 1–25 (1994).